Vibration Reduction and Power Generation with Piezoceramic Sheets Mounted to a Flexible Shaft

P. J. SLOETJES* AND A. DE BOER

Department of Applied Mechanics, University of Twente, 7500AE Enschede, The Netherlands

ABSTRACT: A flexible shaft with surface-mounted piezoceramic sheets and strain sensors is considered which suffers from resonance and self-excited vibration. Frequency domain models, time domain simulations, and control experiments are used to analyze active modal damping and active modal balancing methods. The generation of electric power from cyclic straining of rotor-fixed piezoelectric material is studied and several self-powering devices for condition monitoring and vibration control are proposed.

Key Words: rotor dynamics, piezoelectric actuators, active damping, active balancing, power harvesting.

INTRODUCTION

FAST rotating flexible shafts may exhibit severe bending vibrations and may induce vibration, wear, and noise in their support structures. These problems can often be solved by improving the rotor balance and support damping by passive means. In cases where these means are exhausted, active control methods for rotor balancing and damping provide a solution. Such methods have been the topic of research for a few decades (Sahinkaya and Burrows, 1985; Knospe et al., 1995; Zhou and Shi, 2001).

In recent years, several authors investigated the control of vibrations of flexible rotors by means of rotor-fixed piezoelectric ceramics (Song et al., 2002; Kunze et al., 2003; Kurnik and Przybylowicz, 2003; Przybylowicz, 2003; Horst and Wölfel, 2004). Horst and Wölfel (2004) demonstrated the effectiveness of this approach for a high speed flexible rotor with a heavy disk fixed at one end. They validated a finite element rotor model containing damping, gyroscopic effects, and actuation forces by experiments and used a modal feedback control method to suppress rotor vibration. Kunze et al. (2003) investigated vibration control of an automotive shaft which vibrated in its first bending mode due to excitation from the engine. They equipped a shaft with piezoelectric fiber actuators and sensors and reduced the vibration and resulting vehicle interior noise by positive position feedback control. Slipring assemblies were employed in both experimental setups for data and power transmission. Przybylowicz (2003) presented studies on nonlinear models of thin-walled rotating shafts with piezoelectric sensing and actuation layers. These shafts were destabilized by axial follower forces or axial torques and by rotor damping. Certain combinations of position and velocity feedback control were found to be stabilizing. Song et al. (2002) studied vibration and stability control of a composite shaft. They focused on the relation between structural tailoring and piezoelectric actuation and did not consider any dissipation.

The present research focuses on ways to supply flexible rotors with piezoelectric functionality by taking full advantage of the distinctive properties of piezoceramics: their high stiffness, power density and efficiency, their capability to apply forces in the absence of external supports, and their ability to generate electric power from strain excitation. Emphasis is on the suppression of unbalance induced vibration using rotor-fixed actuators and sensors. Several active vibration control methods are analyzed by means of frequency domain models, time domain simulations, and experiments. In addition, it is studied whether useful amounts of power can be obtained from the periodic straining of rotor-fixed piezoceramics.

ROTOR APPLICATION AND MODEL

As an application, a down-scaled model of a helicopter tail drive shaft is considered which features problematic vibration in its first bending mode. The model shaft is an aluminum tube with a hollow square cross-section (length 1000 mm, width 8–10 mm, weight 100 g), which is connected by flexural couplings to short

*Author to whom correspondence should be addressed.
E-mail: p.j.sloetjes@ctw.utwente.nl
Figures 1 and 10 appear in color online: http://jim.sagepub.com

1045-389X/08/01 0025–10 $10.00/0 DOI: 10.1177/1045389X06072753

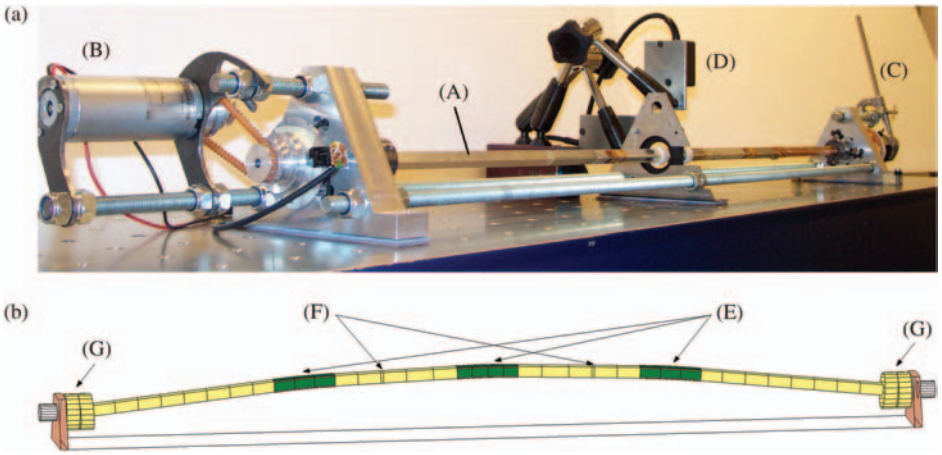

Figure 1. *(a) Experimental setup with shaft (A), motor (B), slipring assembly (C), and laser distance sensors (D) and (b) finite element model showing actuator induced bending deformation and actuators (E), sensors (F) and couplings (G).*

shafts that rotate in ball bearings (Figure 1(a)). The ball bearings are supported by stiff aluminum hole hinge mechanisms which can be supplied with rigid or viscoelastic material in order to modify their damping and stiffness. A catcher bearing at midshaft limits the deflection of the shaft to 1.9 mm. The shaft is driven by an electric motor and drives a slipring assembly. Piezoceramic sheets (dimensions $74 \times 8 \times 0.5\,\text{mm}^3$, weight 36 g, PXE-5 from Morgan Electro Ceramics) are mounted to four sides of the shaft at three positions along its length by means of thin layers of conductive epoxy. The sheets are connected in parallel for each of the two bending planes, such that the displacement pattern shown in Figure 1(b) can be induced in these planes by regulating two voltages. The midshaft deflection is 1.1 μm per volt. Two strain sensor bridges are mounted to the shaft, which are wired so as to measure strains due to symmetric bending modes. The experimental setup is completed by voltage amplifiers, an optical sensor for speed measurement, and a digital control system. Two laser distance sensors are used for direct measurements of the rotor midshaft position and for calibration of the strain sensors.

Rotor Modal Model

The main classes of rotor models which are found in the literature are continuous models (e.g., Przybylowicz, 2003), finite element or transfer matrix models (e.g., Genta, 1998) and lumped parameter models (e.g., Zhou and Shi, 2001). In the present research, a finite element model is employed.

Consistent mass and stiffness matrices for the rotor are obtained by modeling it with modified Timoshenko beam elements as defined in Genta (1998). From the loss factors of the rotor materials, a structural damping matrix is computed. The very small gyroscopic effects as well as torsion and elongation of the rotor are neglected.

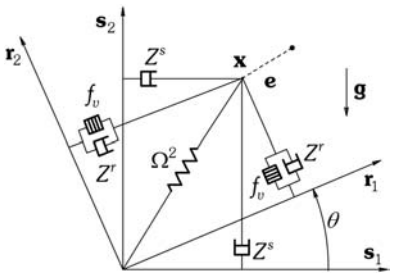

Figure 2. *Vector frames and modal parameters.*

The properties of the bearings and supports are described by lumped stiffness and damping coefficients which give rise to stiffness and viscous damping matrices for the stator. A vector with nodal unbalance loads is assumed and a nodal force vector for unit actuation voltage is computed from the piezoelectric actuator distribution. The transformation method described in Sawicki and Genta (1990) is used to obtain a reduced modal model with viscous damping.

For the analysis, two vector frames are employed which are orthogonal to the rotor rotation axis (see Figure 2). The inertial frame $s = \{\mathbf{s}_1, \mathbf{s}_2\}$ is fixed to the stator, while the non-inertial frame $r = \{\mathbf{r}_1, \mathbf{r}_2\}$ has the same orientation as all rotor cross-sections. Superscripts s and r refer to these frames. For the considered flexible rotor with symmetric supports, the properties of the stator and the rotor can be considered axisymmetric. Analysis is restricted to one bending mode with natural frequency Ω. The participation of this mode is denoted by a vector $\mathbf{x}^s = x_1^s \mathbf{s}_1 + x_2^s \mathbf{s}_2$, which is rewritten as a complex number $\mathbf{x}^s = x_1^s + i x_2^s$, with $i^2 = -1$. A spatial rotation $\mathbf{r}_n = e^{i\theta} \mathbf{s}_n$ $(n = 1, 2)$ relates the two frames, where $e^{i\theta}$ denotes the exponential function and θ is the rotor rotation angle. The influence of angular acceleration $\ddot{\theta}$ is neglected and a normalized semi-constant speed $\omega = \dot{\theta}/\Omega$ is defined.

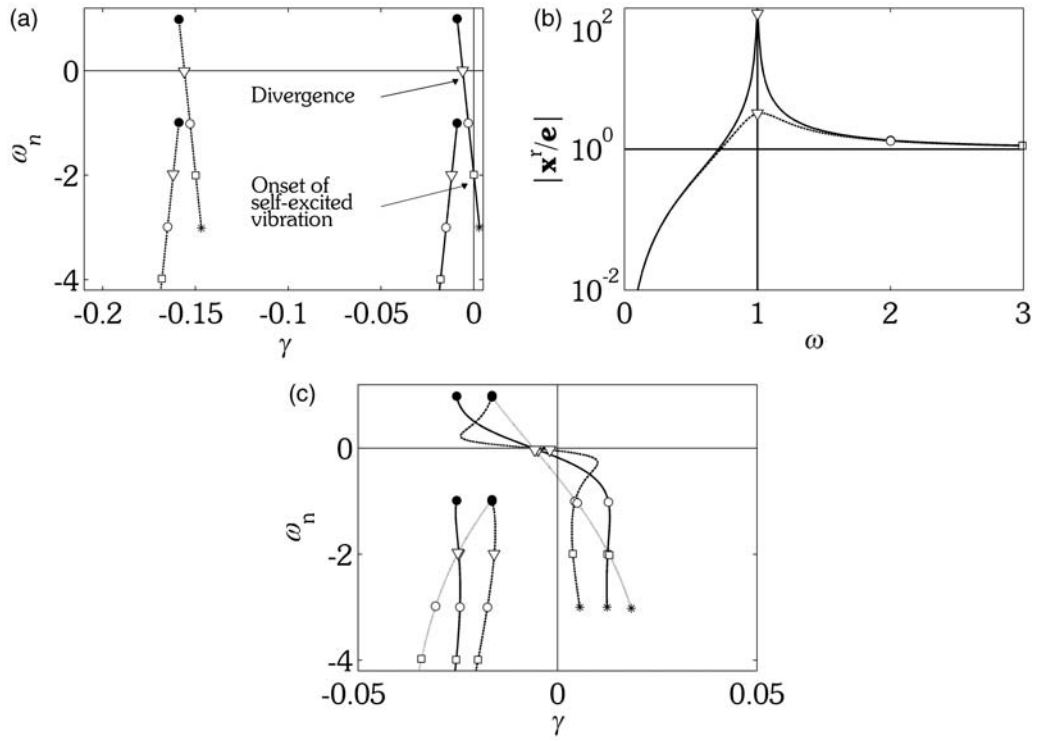

Figure 3. *Example case with $\zeta^s = 6 \times 10^{-3}$ and $\zeta^r = 3 \times 10^{-3}$. For Equations (2) (–), (2) & (5) (- -) with $\zeta^d = 0.15$: (a) λ_n, (b) $|\mathbf{x}^r/\mathbf{e}|$. For Equations (2) & (3) with $f_{RC} = 1$ (–), 1/4(- -), 4 (···): (c) λ_n. Markers: $\omega = 0$ (•), $\omega = 1$ (▽), $\omega = 2$ (○), $\omega = 3$ (□), $\omega = 4$ (∗).*

The modal forces acting at the geometric center $\mathbf{x}$ are modal stiffness Ω^2 times $\mathbf{x}$, modal stator damping Z^s times $\dot{\mathbf{x}}^s$, modal rotor damping Z^r times $\dot{\mathbf{x}}^r$, modal weight factor f_g times gravitational acceleration $\mathbf{g}$, speed $\omega\Omega$ squared times modal eccentricity $\mathbf{e}$, and modal actuation force factor f_v (taking account of the indirect piezoelectric effect) times actuation voltages $\mathbf{v} = v_1^r + iv_2^r$. The voltage $\mathbf{v}$ is assumed to be supplied by a powerful amplifier, such that the actuator charging dynamics are fast and need not be modeled. The modal damping is expressed in terms of damping ratios ζ^s and ζ^r as $Z^s = 2\Omega\zeta^s$ and $Z^r = 2\Omega\zeta^r$. The equation of motion for the first bending mode in the inertial frame is similar to the classical Jeffcott rotor model (see e.g., Genta, 1998):

$$\ddot{\mathbf{x}}^s + 2\Omega(\zeta^s + \zeta^r)\dot{\mathbf{x}}^s + \Omega^2(1 - 2i\omega\zeta^r)\mathbf{x}^s = f_g\mathbf{g} + \omega^2\Omega^2 e^{i\theta}\mathbf{e} + f_v e^{i\theta}\mathbf{v}. \quad (1)$$

Kinematic transformation to the rotating frame yields:

$$\ddot{\mathbf{x}}^r + 2\Omega(\zeta^s + \zeta^r + i\omega)\dot{\mathbf{x}}^r + \Omega^2(1 - \omega^2 + 2i\omega\zeta^s)\mathbf{x}^r = f_g e^{-i\theta}\mathbf{g} + \omega^2\Omega^2\mathbf{e} + f_v\mathbf{v}. \quad (2)$$

In the absence of voltage regulation, the voltages which are induced upon straining of the actuators cannot be neglected, since electric currents will flow and be dissipated if resistances R are connected to the actuators having capacitances C. The following equation can be written for the free voltage $\mathbf{v}$, with $f_{RC} = (\Omega RC)^{-1}$ the normalized frequency of the electric RC-circuit:

$$\dot{\mathbf{v}} + \Omega f_{RC}\mathbf{v} = \Omega f_{RC} f_v \mathbf{x}^r. \quad (3)$$

The present model does not contain inductive effects, because these are negligible for small capacitances.

Dynamics Uncontrolled Rotor

Substitution of $\mathbf{x}^r = e^{\lambda_n(\omega)t}\mathbf{x}_0^r$ in the homogeneous Equation (2) yields eigenvalues $\lambda_n(\omega) = \Omega(\gamma_n(\omega) + i\omega_n(\omega))$, $(n = 1, 2)$. The imaginary parts $i\omega_n$ represent circular motion with normalized whirl speed ω_n in the rotating frame, while the real parts γ_n represent time decay if negative. An example case is defined with damping ratios $\zeta^s = 0.006$ and $\zeta^r = 0.003$. For this case, the eigenvalue trajectories of Equation (2) are shown as solid lines in Figure 3(a).

The dependence of the system on ω gives rise to resonance and self-excited vibration. Resonance is said to occur when $\mathbf{x}^r(\omega)/\mathbf{e}$, the transfer from modal unbalance to modal position at constant speed, attains its maximum, which is the case at the critical speed $\hat{\omega} = (1 + 4\zeta^{s2})^{1/2} \approx 1$ (Figure 3(b)). Self-excited vibration starts as soon as the destabilizing orthogonal stiffness effect of rotor damping exceeds the stabilizing effect of

both rotor and stator damping. Hence, at speeds exceeding the onset speed of unstable vibration $\omega_f = 1 + \zeta^s/\zeta^r$, a spiral motion with whirl speed $\Omega(1-\omega)$ occurs. In the example case, ω_f is 3 (see Figure 3(a)).

The influence of electric dissipation is determined by considering Equations (2) & (3). Figure 3(c) shows the eigenvalues of this system for $f_{RC} = 1/4$, $f_{RC} = 1$, and $f_{RC} = 4$. Maximum current dissipation occurs at $|\omega_n(\omega) - \omega| \approx f_{RC}$. Two maxima are present if $f_{RC} < 1$. Note that, in general, electric current dissipation reduces the onset speed of self-excited vibration. Circuits connected to the actuator electrodes should have either very low or very high impedances if significant dissipation is to be avoided.

VIBRATION CONTROL METHODS

For the suppression of resonant vibration or unstable vibration, active modal damping in the form of negative modal position derivative feedback can often be used (Preumont, 1997). For the reduction of unbalance induced vibration at arbitrary speed, modal balancing methods are most suitable (Zhou and Shi, 2001).

Active Modal Damping

Modal damping takes the following shape for a setup in which sensors on the stator are used to measure the distance to the rotor surface:

$$\mathbf{y}^s = q^s \mathbf{x}^s \tag{4a}$$

$$\mathbf{v} = -k_d \Omega e^{-i\theta} \frac{\mathrm{d}}{\mathrm{d}t} \mathbf{y}^s \tag{4b}$$

with q^s the modal sensitivity of the distance sensors, $\mathbf{y}^s$ the distance measurement, k_d a feedback gain normalized to Ω, d/dt an explicit time derivative, θ the measured rotor rotation angle, and $e^{-i\theta}$ the transformation to the voltage $\mathbf{v}$ over the rotating actuators.

For a system with rotor-fixed strain sensors, Equation (4) must be transformed to the rotating frame. This yields:

$$\mathbf{y}^r = q^r \mathbf{x}^r \tag{5a}$$

$$\mathbf{v} = -k_d \Omega \left(\frac{\mathrm{d}}{\mathrm{d}t} \mathbf{y}^r + i\omega\Omega \mathbf{y}^r \right) \tag{5b}$$

with q^r the modal sensitivity of the strain sensors, $\mathbf{y}^r$ the measurement signals, and ω the measured rotor speed. A gain $k_d = 0.3$ is selected in the example case, which leads to an 'active modal damping ratio' ζ^d of 0.15. The eigenvalue trajectories of Equations (2) & (5) are shown as dotted lines in Figure 3(a). Since $\zeta^d \gg \zeta^s$, the apparent support damping is significantly increased and self-excited vibration is postponed from $\omega > 3$ to $\omega > 53$. The response to unbalance at $\hat{\omega}$ is reduced by 96% (dotted line in Figure 3(b)). (Note that most self-exciting mechanisms could be compensated with very little effort using strain derivative feedback only if the feedback gain were adapted to achieve stability).

In practice, the explicit time derivative in Equation 5(b) amplifies high-frequency sensor noise. This effect is reduced by adding low-pass filters with corner frequencies $f_l\Omega$, such that low-pass filtered measurements $\mathbf{y}_l^r$ are obtained:

$$\frac{\dot{\mathbf{y}}_l^r}{f_l\Omega} + \mathbf{y}_l^r = q^r \mathbf{x}^r \tag{6a}$$

$$\mathbf{v} = -k_d \Omega \left(\frac{\mathrm{d}}{\mathrm{d}t} \mathbf{y}_l^r + i\omega\Omega \mathbf{y}_l^r \right). \tag{6b}$$

The eigenvalue trajectories of Equations (2) & (6) for the example case with $f_l = 2.0$ are shown in Figure 4(a) (one trajectory of overdamped eigenvalues is not visible). Comparison with Figure 3(a) learns that, due to low-pass filtering, the effect of active damping reduces with increasing whirl speed $\omega_n(\omega)$. Since at resonance, $\omega_n(\omega)$ is near to zero, the only condition for effective resonance suppression is that the $f_l\Omega$ are sufficiently high with respect to the rate of change in the response to unbalance.

In the case of rotors which accelerate only slowly and have largely axisymmetric support properties, resonance due to unbalance can be effectively suppressed even if the time derivative in Equation 6(b) is neglected, f_l in Equation 6(a) is made very small and ω is replaced

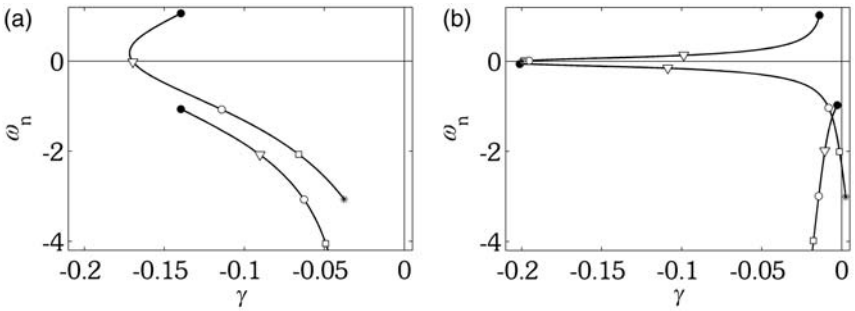

Figure 4. *(a) Eigenvalue Equations (2) & (6), $k_d = 0.3$, $f_l = 2.0$ and (b) Eigenvalue Equations (2) & (7), $k_d = 0.3$, $f_l = 0.2$. Markers: $\omega = 0$ (•), $\omega = 1$ (∇), $\omega = 2$ (○), $\omega = 3$ (□), $\omega = 4$ (∗).*

by unity. The resulting constant gain feedback law increases the orthogonal stiffness for slow motion only:

$$\frac{\dot{\mathbf{y}}_l^r}{f_l\Omega} + \mathbf{y}_l^r = q^r \mathbf{x}^r \tag{7a}$$

$$\mathbf{v} = -ik_d\Omega^2 \mathbf{y}_l^r. \tag{7b}$$

Application of this law is referred to as orthogonal position feedback. The eigenvalue trajectories of Equations (2) & (7) with $f_l = 0.2$ are shown in Figure 4(b). The response to unbalance is nearly equal to that of Equations (2) & (5). The system of Equations (2) & (7) is conditionally stable. For $k_d = 0.3$, stability at $\omega = 0$ is guaranteed only for $f_l < 0.24$, hence the use of low pass filters is crucial. This control law is effective near critical speeds only.

It is noted that Equations 6(b) and 7(b) can be used for active damping in the presence of large support stiffness anisotropy as long as the flexibility of the symmetric rotor is dominant. In general, the effect of stiffness anisotropy diminishes with increasing damping (Genta, 1998).

Active Resonance Suppression

The use of rotor-fixed sensors has definite drawbacks. First, note the cross-coupling ($\mathbf{v} \sim i$) in Equations (5)–(7), which may lead to phase inaccuracies in case the gains of sensors or amplifiers are not equal for the two principal directions. Second, note the dependency on absolute modal position ($\mathbf{v} \sim \mathbf{x}^r$) in Equations (5)–(7), which may lead to problems with sensor offset drift. This is particularly problematic with symmetric rotor systems for which the response to unbalance at constant speed is largely constant in the rotating frame. (Note that offset drift does not complicate stability control using rotor-fixed sensors, because self-excited vibration leads to periodic straining of the rotor). A control system which employs rotor-fixed sensors must therefore in general cope with offset drift. To address this problem, a slowly time-varying unknown offset $\mathbf{o}(t)$ is introduced in the sensor equation:

$$\frac{\dot{\mathbf{y}}_l^r}{f_l\Omega} + \mathbf{y}_l^r = q^r(\mathbf{x}^r + \mathbf{o}(t)). \tag{8}$$

The following offset estimation algorithm is defined:

Algorithm O: A gain $\delta_o(\omega)$ is changed from 0 to 1 at speeds ω for which $\mathbf{x}^r(\omega)/\mathbf{e}$ is small. While $\delta_o(\omega) = 1$, the low-pass filtered measurement $\mathbf{y}_l^r$ is simply attributed to $\mathbf{o}$ by computing an offset estimate $\underline{\mathbf{o}}$ as the recursive least squares (RLS) estimate of $\mathbf{y}_l^r$:

$$\text{while } (\delta_o(\omega) > 0) \quad \underline{\mathbf{o}} = RLS\{\underline{\mathbf{o}}, \mathbf{y}_l^r\}. \tag{9}$$

Initial sensor offsets are corrected by diminishing $\mathbf{y}_l^r$ by $\underline{\mathbf{o}}$. Although drift occurring after offset estimation limits the period during which this estimate can be used, a sufficiently long period should be feasible in many cases.

Algorithms for the suppression of resonance may be scheduled with respect to the rotor speed as well. The following algorithm is based on Equation 6(b):

Algorithm S: Orthogonal position feedback is applied while ω is near to $\hat{\omega}$ by means of a gain $\delta_d(\omega)$, $0 \le \delta_d \le 1$:

$$\mathbf{v} = -i\delta_d(\omega)k_d\Omega^2(\mathbf{y}_l^r - \underline{\mathbf{o}}). \tag{10}$$

Application of this algorithm yields a low-frequency control action which suppresses resonance.

Modal balancing methods are usually implemented with low-frequency actuators and algorithms as well (Zhou and Shi, 2001). The advantage of these is their low power consumption and computational burden, respectively. Two more low-frequency algorithms for the suppression of resonance are defined in the following lines (their performance is analyzed in the next sections):

Algorithm I: Negative integral feedback with gain k_i is applied while $\omega < \hat{\omega}$. The integral is kept constant and used for open loop control while $\omega \ge \hat{\omega}$. To achieve this, gains $\delta_Y(\omega)$ and $\delta_i(\omega)$ are defined. Both gains are made nonzero while $\omega < \hat{\omega}$, but $\delta_i(\omega)$ is made nonzero while $\omega \ge \hat{\omega}$ as well:

$$\mathbf{Y} = \int \delta_Y(\omega)(\mathbf{y}_l^r - \underline{\mathbf{o}})\mathrm{d}t \tag{11a}$$

$$\mathbf{v} = -\delta_i(\omega)k_i\mathbf{Y}. \tag{11b}$$

Algorithm B: While ω is not far from $\hat{\omega}$, a gain $\delta_e(\omega)$ is used to start the computation of an unbalance estimate $\underline{\mathbf{e}}$ from the measurement $\mathbf{y}_l^r$ using the inverse transfer function of the undamped system. While ω is near to $\hat{\omega}$, gain $\delta_e(\omega)$ is again set to zero but a gain $\delta_b(\omega)$ is made nonzero to apply a voltage which should balance the rotor:

$$\text{while} \quad (\delta_e(\omega) > 0)\underline{\mathbf{e}} = RLS\left\{\underline{\mathbf{e}}, \frac{(\mathbf{y}_l^r(\omega) - \underline{\mathbf{o}})}{1 - \omega^2}\right\} \tag{12a}$$

$$\mathbf{v} = -\delta_b(\omega)\frac{\Omega^2\,\underline{\mathbf{e}}}{f_v\,q^r}. \tag{12b}$$

Equation 12(b) indicates that modal balancing of flexible rotors using rotor-fixed piezoelectric actuators is in fact achieved by rotor shape control. For a targeted mode with worst case modal eccentricity $\mathbf{e}_{\max}$, the actuators should at least be able to apply a modal force $\mathbf{f}_{\min} = -\Omega^2\mathbf{e}_{\max}$. Note that a high actuator-to-rotor mass ratio can be required to balance a lightweight rotor made of a stiff material by means of shape control. On the other hand, a flexible rotor with heavy attached components might often be

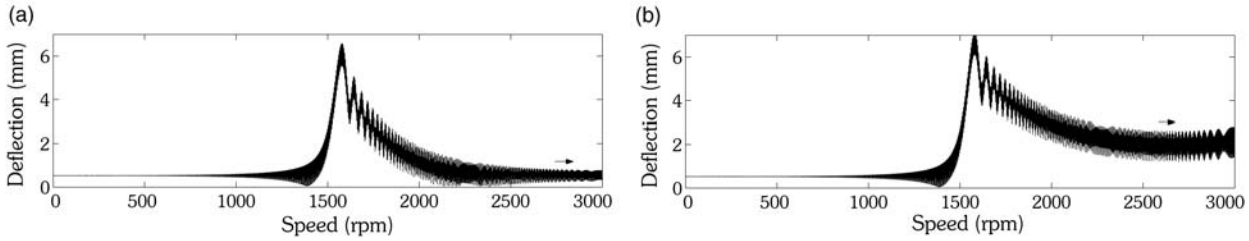

Figure 5. *Deflection amplitude of numerical model with: (a) $\zeta^s = 2.4 \times 10^{-3}$, $\zeta^r = 0.9 \times 10^{-3}$ and (b) $\zeta^s = 1.3 \times 10^{-3}$, $\zeta^r = 1.7 \times 10^{-3}$.*

balanced using a relatively small amount of piezoelectric material.

SIMULATIONS OF VIBRATION CONTROL

For analysis in the time domain, a modal model containing two pairs of modes is derived from the rotor finite element model. The static response of the remaining modes is taken into account in order to obtain accurate results in non-resonance conditions. On the basis of this modal model, a state space model is defined which is integrated in time using a Runge–Kutta 4.5 integration scheme. To make the simulations more realistic, slight deviations from axial symmetry are introduced in the support stiffness and white noise is added to the sensor signals. The frequency of the first mode is 25.8 Hz. The first modal unbalance is equivalent to a point unbalance of 5.7×10^{-6} kg m at midshaft in $\{\mathbf{r}_1, -\mathbf{r}_2\}$ direction. The modal unbalance which is introduced by actuation is equivalent to 4.0×10^{-8} kg m per volt at midshaft. In all simulations, the transient response is computed for a run-up from 0 to 3000 rpm in 30 s.

Simulations of Uncontrolled Rotor

Two cases with different damping coefficients are considered: (a) high support damping and low rotor damping ($\zeta^s = 2.4 \times 10^{-3}$, $\zeta^r = 0.9 \times 10^{-3}$) and (b) low support damping and high rotor damping ($\zeta^s = 1.3 \times 10^{-3}$, $\zeta^r = 1.7 \times 10^{-3}$). The magnitude of the rotor deflection at midshaft (after transformation to the stationary frame) is shown in Figure 5(a) and (b). Note that the rotor deflects 45 μm under gravity, that in both cases a rather large resonant response is present due to unbalance and that the rotor is stable until at least 3000 rpm in the first case while self-excited vibration starts at 2730 rpm in the second case.

Simulations of Rotor Vibration Control

The suppression of resonance using four combinations of algorithms S, I, and B is simulated for the first case with $\zeta^s = 2.4 \times 10^{-3}$ and $\zeta^r = 0.9 \times 10^{-3}$.

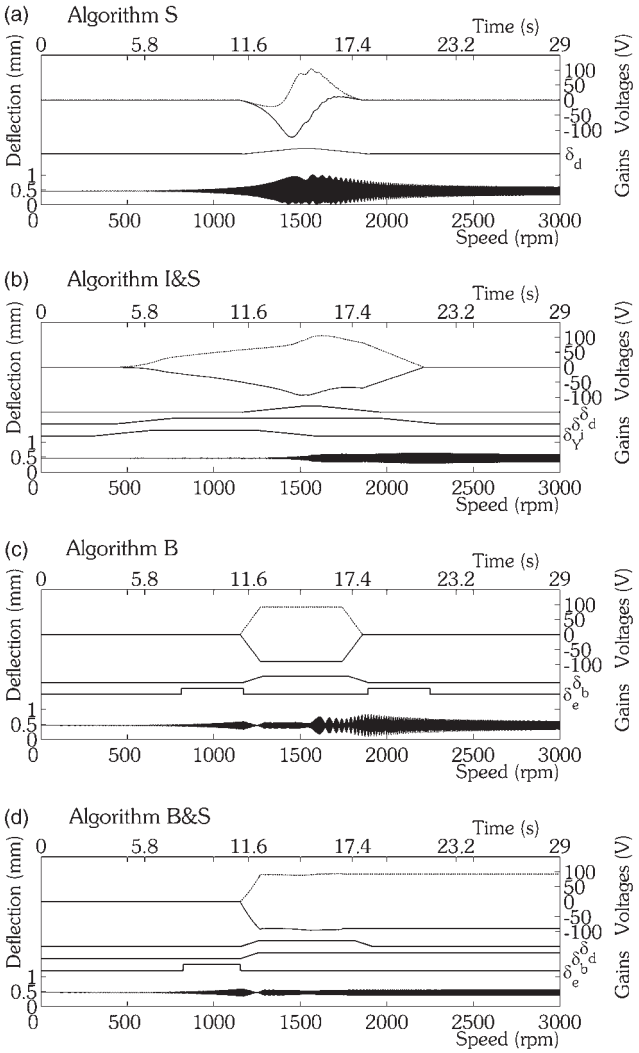

Figure 6. *Results from control simulations with algorithms (a)–(d). Midshaft deflection (bottom). Actuation voltages v_1 (---), v_2 (—) (top). Scheduling gains δ (center).*

Sensor drift is assumed to be absent and offset estimation is not simulated ($\delta_o = 0$). In Figure 6, the rotor deflection is shown at the lower part of the plot, the two actuation voltages in the upper part of the plot, and the scheduling gains in the center of the plot.

Algorithm S: Figure 6(a). Orthogonal position feedback near the critical speed is already quite effective.

Note that the actuation voltages vary only slowly since the response to unbalance changes slowly in the rotating frame.

Algorithm I and S: Figure 6(b). A combination of negative integral feedback below the critical speed and open loop integral feedback with orthogonal position feedback at the critical speed effectively suppresses resonance.

Algorithm B: Figure 6(c). Scheduled unbalance estimation and balancing leave a small residual unbalance response at the critical speed. This is due to the unbalance estimation algorithm neglecting support damping and contributions of modes other than the first mode.

Algorithm B and S: Figure 6(d). Scheduled balancing near and after the critical speed and orthogonal position feedback at the critical speed lead to nearly perfect self-centering over the complete speed range.

EXPERIMENTS WITH VIBRATION CONTROL

Experiments with Uncontrolled Rotor

The properties and response of the rotor setup were determined by modal analysis and transient analysis. The frequency of the first bending mode was 25.4 Hz, near the predicted value of 25.8 Hz. Approximate damping ratios were determined for different conditions of the rotor and supports. An estimate of the support damping in the 'low damping' condition ($\zeta^s \approx 1.3 \times 10^{-3}$) was obtained by combining the total damping ratio for a rotor without actuators at zero speed ($\zeta^s + \zeta^r \approx 1.6 \times 10^{-3}$) with the fact that it allowed stable rotation up to at least 8400 rpm. The supports were supplied with viscoelastic material to obtain their 'high damping' condition ($\zeta^s \approx 2.4 \times 10^{-3}$). The rotor in the 'low damping' condition had its actuator electrodes short-circuited ($\zeta^r \approx 0.9 \times 10^{-3}$), while these were connected to voltage amplifiers regulating 0 V in the 'high damping' condition ($\zeta^r \approx 1.7 \times 10^{-3}$). As no passive balancing cycle was performed after assembly of the rotor, rather much unbalance was present. The first modal unbalance had the same direction and nearly equal magnitude as mentioned for the numerical simulations.

The transient response is again presented for two cases: (a) high support damping with low rotor damping and (b) low support damping with high rotor damping. Figure 7 shows the magnitude of the midshaft deflections as estimated from the strain sensor measurements during runs from 0 to 3000 rpm in 30 s. (The influence of gravity was filtered out from the rotor strain measurements, for clarity of the figure). In both cases, the midshaft deflection was clearly limited by the catcher bearing. In the second case, the rotor was only marginally stable at high speeds.

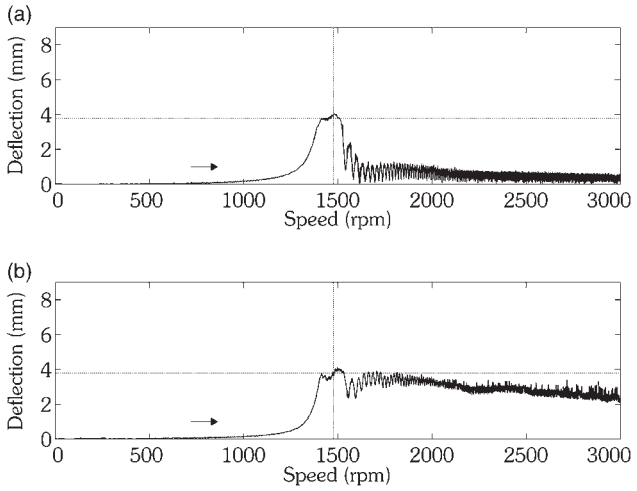

Figure 7. *Deflection amplitude of experimental setup with (a) $\zeta^s \approx 2.4 \times 10^{-3}$, $\zeta^r \approx 0.9 \times 10^{-3}$, (b) $\zeta^s \approx 1.3 \times 10^{-3}$, $\zeta^r \approx 1.7 \times 10^{-3}$. Vertical line: $\hat{\omega}$. Horizontal line: catcher bearing.*

Experiment with Stabilization

In a subsequent experiment, the support damping was reduced to an even lower value ($\zeta^s \approx 1.0 \times 10^{-3}$) by modifying the support mounts. In this condition, the rotor with short-circuited actuators was still stable up to at least 4200 rpm, but the rotor with actuators connected to the amplifiers at 0 V exhibited unstable bending vibration at speeds exceeding 2460 rpm. Since ideal voltage amplifiers regulating 0 V would behave like short-circuits, the amplifiers are likely to be non-ideal in the sense that they dissipate the charges which are produced in the actuators upon straining, leading to increased rotor damping (compare Figure 3(c)). The unstable vibration was actively stabilized with low effort using a controller implementation of Equation 6(b). For vibration control of marginally stable rotors, it is sensible to use charge amplifiers or voltage amplifiers with very high impedance to avoid dissipation.

Experiments with Rotor Vibration Control

Experiments with the suppression of unbalance induced vibration were performed for the case with high stator damping, where the sensor offset was estimated at speeds up to 60 rpm. The magnitude of the midshaft deflection, the scheduling gains, and the actuation voltages are shown in Figure 8. Note that the actuation voltages are quite similar to those obtained by numerical simulation. The best result was achieved with

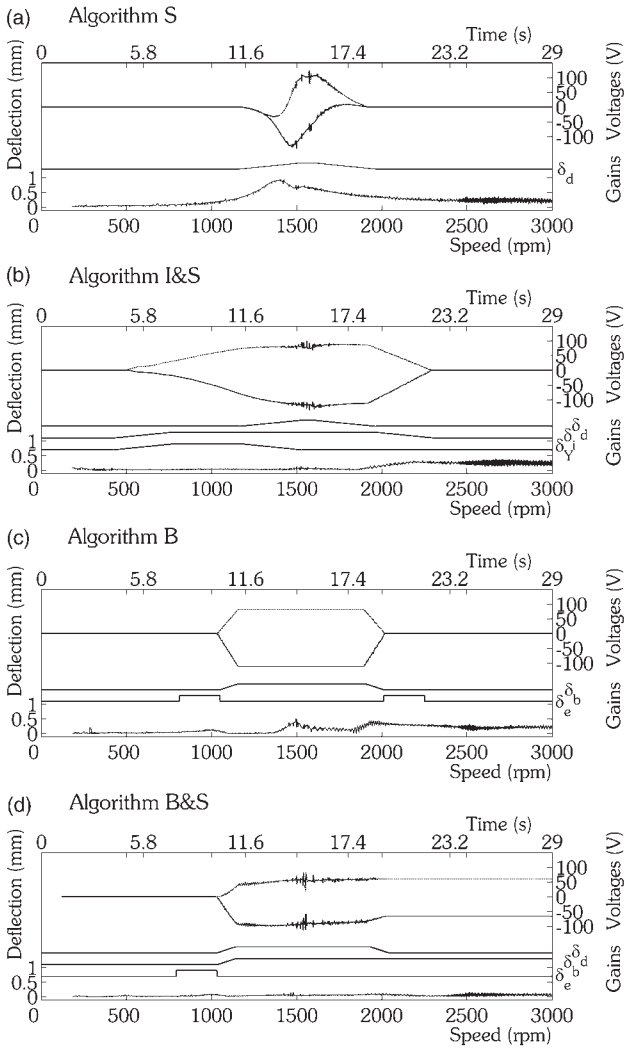

Figure 8. *Results from control experiments with algorithms (a) to (d). Midshaft deflection (bottom). Actuation voltages v_1 (---), v_2 (—) (top). Scheduling gains δ (center).*

algorithm (*d*), which reduced the maximum midshaft deflection from 3800 to 120 μm: a reduction of 97%.

EXTRACTION OF ELECTRIC POWER

Piezoelectric material which experiences periodic strains can be used as a power source (Sodano et al., 2004). Piezoceramic material which is mounted to the surface of a flexible rotor experiences strains which vary harmonically in time during rotation due to bending of the rotor under its own weight. Piezoceramic material on a rotor may hence function as a power source which, in contrast to batteries or electromagnetic generators, is both permanent and compact. A disadvantage is that power extraction increases the rotor damping and hence reduces the onset speed of self-excited vibration. Yet, in most practical cases, the support damping is large

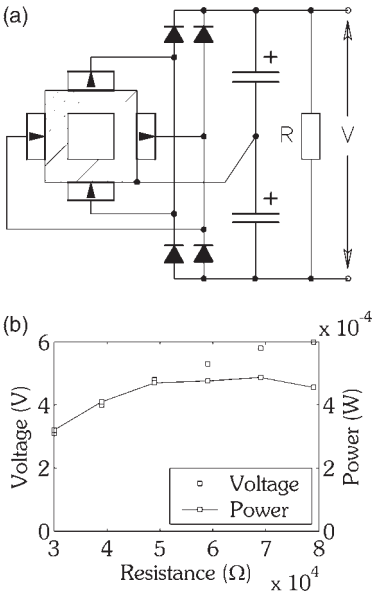

Figure 9. *(a) Circuit for power dissipation measurement and (b) voltage and power as a function of load resistance R at 3600 rpm.*

enough with respect to the introduced dissipation to avoid instability.

Experiment with Power Extraction

The maximum amount of electric power $P_{\max}$ which can be generated by harmonic straining is approximately equal to (see Roundy, 2005):

$$P_{\max} = \lambda_{\max}\omega 2E^g_{\max} = \frac{k^2_{31}}{2-k^2_{31}}\omega E^g_{\max} \qquad (13)$$

with $k_{31} = 0.38$ the piezoelectric coupling factor and $E^g_{\max} = 15\,\mu\text{Ws}$ the maximum strain energy in the piezoceramic material in one bending plane due to bending under gravity, which follows from the finite element model. It follows that 0.45 mW can be extracted at a speed of 3600 rpm. For validation, experiments were conduced with the circuit in Figure 9(a), which rectifies the induced currents, charges two capacitors of 47 μF, and discharges these through a resistance *R*. According to Figure 9(b), a resistance of 70 kΩ maximized the dissipated power at 0.48 mW, which corresponds quite well to the prediction. The extraction of electric power resulted in unstable vibration in the 'low support damping' condition.

The amount of power which can be extracted from the model shaft would enable for example, wireless measurements of strain at a rate of a few Hertz for condition monitoring purposes (Arms et al., 2005). More demanding condition monitoring applications might be realized in the case of larger flexible shafts, especially if piezoelectric fiber composites with a higher coupling constant would be employed (Chopra, 2000).

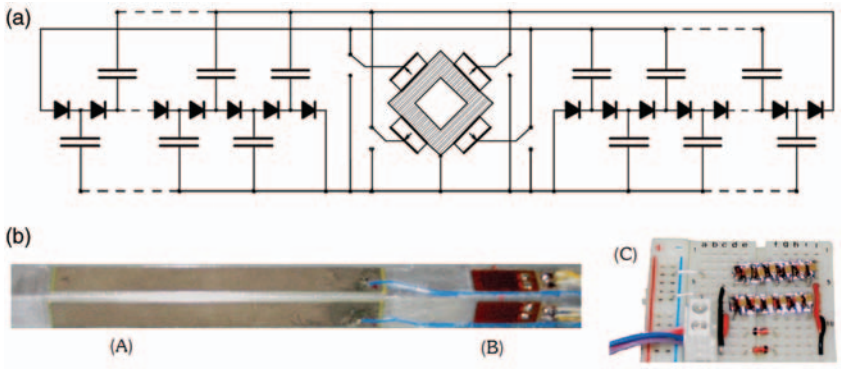

Figure 10. *(a) Multiplier circuit which charges the actuators to high voltages and (b) shaft with (A) piezoelectric actuators, (B) strain sensors, and (C) board with voltage multipliers.*

Storing power in a modern double layer capacitor during a longer period of rotation would for example enable integrated devices for structural health testing to be run periodically.

Experiment with High Voltage Generation

With locally generated power, limited vibration control functions could be realized as well. From Figure 8, the conclusion can be drawn that the different algorithms for resonance suppression require only a single actuator charge–discharge cycle. The actuators on the shaft have a summed capacity of 270 nF and can all be charged to for example 50 V using only 0.34 mWs. This amount of energy is small compared to the 0.48 mW which can be extracted at 3600 rpm. The low harmonic voltages induced by straining could be transformed directly into the high voltages which are required for actuation by means of voltage multiplier circuits. An example circuit with two times three multiplier stages is shown in Figure 10(a). This circuit continuously charges the actuators to positive and negative constant high voltages during rotation. A first experiment was conducted with two six-stage voltage multipliers that were assembled from standard diodes and multilayer ceramic capacitors of 100 nF (see Figure 10(b)). At a speed of 3600 rpm, the actuators were charged to more than ± 90 V within 20 s. A run-up to 1500 rpm in 15 s resulted in actuator voltages of ± 40 V. A second experiment with four six-stage multipliers which were connected independently to the actuators on the four sides of the shaft produced similar results. The performance of these circuits could be improved by using components with lower capacities and losses.

SYSTEM LEVEL DEVICE CONCEPTS

The proven effectiveness of vibration control and power generation with rotor-fixed piezoceramics justifies further research on practical devices that extend the functionality of flexible rotors. Four system level concepts of such devices are outlined (see Figure 11):

1. *Condition Monitoring Device*. Charge is extracted from rotor-fixed piezoceramics and is stored on a double layer capacitor. Periodically, the rotor condition is examined and communicated wirelessly to a stationary device for semi real time damage detection.
2. *Resonance Suppression Device*. Charge is extracted from rotor-fixed piezoceramics and is restored at a high voltage. The centripetal acceleration of a rotor-fixed ring is measured with resistive pressure sensors. The sensor resistances determine the voltages to which the actuators are discharged in such a way that resonance is suppressed.
3. *Active Damping Device*. A small induction generator or light source powers a control system on the rotor and supplies it with information on the rotor orientation. Rotor bending is measured with strain sensors and is suppressed by active modal damping.
4. *Wireless Balancing Device*. Charge is extracted from rotor-fixed piezoceramics and is restored at a high voltage. The actuators are discharged by means of switches that are wirelessly controlled by a device which attempts to minimize accelerations measured at the stator.

Further research on these devices should be performed for carefully selected target applications. Self-powering devices can be realized only if significant periodic strains occur in rotor-fixed piezoceramics and sufficient damping is provided by the supports. Modal balancing by rotor shape control is attractive only for sufficiently flexible rotors. Devices which use rotor-fixed sensors must solve any problem with sensor offset drift. In addition, piezoceramic fiber composites might often be preferred over ceramic sheets, because they are more easily mounted to curved surfaces with low diameter.

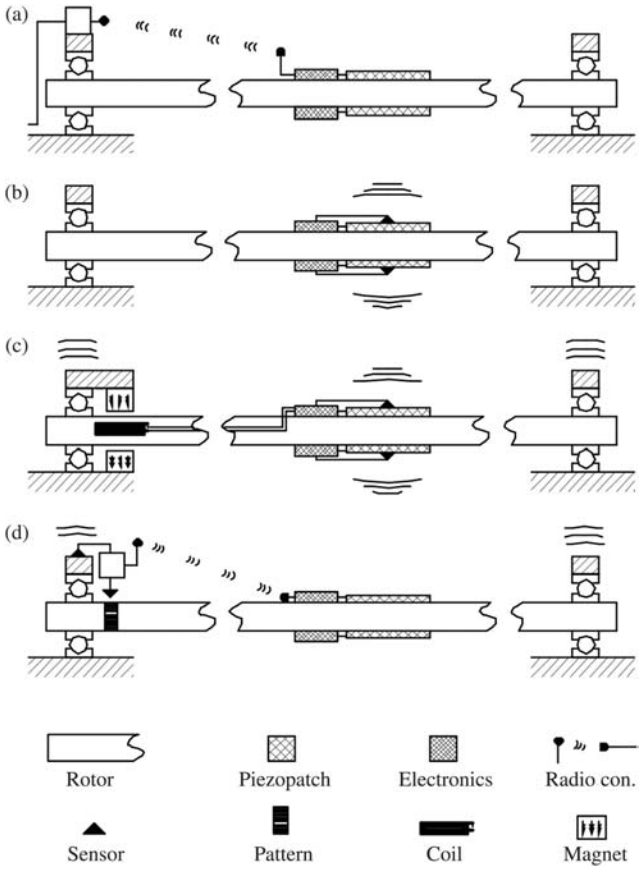

Figure 11. *(a) Condition monitoring device, (b) resonance suppression device, (c) active damping device, and (d) wireless balancing device.*

For all mentioned devices, a good balance should be found between structurally integrated and modular implementations (see also Chopra, 2000).

CONCLUSIONS

A flexible shaft with rotor-fixed piezoceramic actuators and strain sensors was considered. The effectiveness of several low-frequency control algorithms for the suppression of resonance was demonstrated, where good correspondence between simulations and experiments was found. Experiments with the extraction of electric power from the rotor-fixed piezoceramics indicated that self-powering devices with limited condition monitoring and vibration control functions are feasible. On the basis of the results, four innovative system level concepts of flexible rotors with piezoelectric functionality are outlined.

ACKNOWLEDGMENTS

The authors acknowledge the support of the National Aerospace Laboratory NLR.

REFERENCES

Arms, S.W., Townsend, C.P., Churchil, D.L., Galbreath, J.H. and Mundell, S.W. 2005. "Power Management for Energy Harvesting Wireless Sensors," *Proceedings of SPIE*, 5763:267–275.

Chopra, I. 2000. "Review of State of Art of Smart Structures and Integrated Systems," *AIAA Journal*, 40(11):2145–2187.

Genta, G. 1998. *Vibration of Structures and Machines – Practical Aspects*, 3rd edn, Springer-Verlag, Berlin, 2nd edition.

Horst, H.-G. and Wölfel, H.P. 2004. "Active Vibration Control of a High-speed Rotor Using PZT Patches on the Shaft Surface," *Journal of Intelligent Material Systems and Structures*, 15(9):721–728.

Knospe, C.R., Hope, R.W., Fedigan, S.J. and Williams, R.D. 1995. "Experiments in the Control of Unbalance Response Using Magnetic Bearings," *Mechatronics*, 5(4):385–400.

Kunze, H., Riedel, M., Schmidt, K. and Bianchini, E. 2003. "Vibration Reduction on Automotive Shafts Using Piezoceramics," *Proceedings of SPIE*, 5054:382–386.

Kurnik, W. and Przybylowicz, P.M. 2003. "Active Stabilization of a Piezoelectric Fiber Composite Shaft Subject to Follower Load," *International Journal of Solids and Structures*, 40(19):5063–5079.

Preumont, A. 1997. *Vibration Control of Active Structures*, Kluwer Academic Publishers, Dordrecht.

Przybylowicz, P.M. 2003. "Active Stabilization of a Rotating Shaft Transmitting Static Torque," *Meccanica*, 38(6):763–770.

Roundy, S. 2005. "On the Effectiveness of Vibration-based Energy Harvesting," *Journal of Intelligent Material Systems and Structures*, 16(10):809–823.

Sahinkaya, M.N. and Burrows, C.R. 1985. "Control of Stability and the Synchronous Vibration of a Flexible Rotor Supported on Oil-film Bearings," *Journal of Dynamical Systems, Measurement, and Control*, 107(6):139–144.

Sawicki, J.T. and Genta, G. 1990. "Unbalance Response of Rotors: A Modal Approach with Some Extensions to Damped Natural Systems," *Journal of Sound and Vibration*, 140(1):129–153.

Sodano, H.A., Inman, D.J. and Park, G. 2004. "A Review of Power Harvesting from Vibration Using Piezoelectric Materials," *The Shock and Vibration Digest*, 36(3):197–205.

Song, O., Librescu, L. and Jeong, N.-H. 2002. "Vibration and Stability Control of Smart Composite Rotating Shaft via Structural Tailoring and Piezoelectric Strain Actuation," *Journal of Sound and Vibration*, 257(3):503–525.

Zhou, S. and Shi, J. 2001. "Active Balancing and Vibration Control of Rotating Machinery: A Survey," *The Shock and Vibration Digest*, 33(4):361–371.